ELSEVIER

Journal of the Mechanics and Physics of Solids
52 (2004) 2403–2430

JOURNAL OF THE
MECHANICS AND
PHYSICS OF SOLIDS

www.elsevier.com/locate/jmps

A quantum-mechanically informed continuum model of hydrogen embrittlement

S. Serebrinsky[a], E.A. Carter[b], M. Ortiz[a,*]

[a] *Graduate Aeronautical Laboratories, Division of Engineering and Applied Science, California Institute of Technology, Pasadena, CA 91125, USA*

[b] *Department of Chemistry and Biochemistry, University of California at Los Angeles, Los Angeles, CA 90095-1569, USA*

Received 17 August 2003; received in revised form 4 February 2004; accepted 13 February 2004

Abstract

We present a model of hydrogen embrittlement based upon: (i) a cohesive law dependent on impurity coverage that is calculated from first principles; (ii) a stress-assisted diffusion equation with appropriate boundary conditions accounting for the environment; (iii) a static continuum analysis of crack growth including plasticity; and (iv) the Langmuir relation determining the impurity coverage from its bulk concentration. We consider the effect of the following parameters: yield strength, stress intensity factor, hydrogen concentration in the environment, and temperature. The calculations reproduce the following experimental trends: (i) time to initiation and its dependence on yield strength and stress intensity factor; (ii) finite crack jump at initiation; (iii) intermittent crack growth; (iv) stages I and II of crack growth and their dependence on yield strength; (v) the effect of the environmental impurity concentration on the threshold stress intensity factor; and (vi) the effect of temperature on stage II crack velocity in the low-temperature range. In addition, the theoretically and experimentally observed intermittent cracking may be understood as being due to a time lag in the diffusion of hydrogen towards the cohesive zone, since a buildup of hydrogen is necessary in order for the crack to advance. The predictions of the model are in good quantitative agreement with available measurements, suggesting that hydrogen-induced degradation of cohesion is a likely mechanism for hydrogen-assisted cracking.

Keywords: Hydrogen embrittlement; Multiscale modelling; Cohesive theories of fracture; Stress-assisted diffusion; Density-functional theory

* Corresponding author. Fax: +1-626-449-6359.
E-mail address: ortiz@aero.caltech.edu (M. Ortiz).

0022-5096/$ - see front matter
doi:10.1016/j.jmps.2004.02.010

1. Introduction

Stress-corrosion cracking (SCC) and hydrogen embrittlement (HE) are related, long-standing problems, commonly described under the name of environment-assisted cracking (EAC), which remain incompletely understood from the mechanistic point of view. Accordingly, the accurate prediction of the lifetime of engineering components undergoing EAC remains an elusive goal. Owing to its complex nature, a number of widely differing mechanisms of EAC have been proposed (Gangloff and Ives, 1990; Turnbull, 1993; Jones, 2001; Sofronis, 2001). Some of the mechanisms presently under study include: slip-step dissolution (Scully, 1975; Vermilyea, 1977; Parkins, 1990; Ford, 1990); film-induced cleavage (Edeleanu and Forty, 1960; Sieradzki and Newman, 1985, 1987); surface mobility (Galvele, 1987, 2000); and variants of hydrogen embrittlement (Sofronis, 2001; Birnbaum, 1990). The proliferation of models, each consistent with particular sets of experimental data, suggests that all instances of environment-assisted cracking may not be describable by a universal mechanism.

In this work, we focus our attention on systems where HE is recognized to be the principal source of damage, such as high-strength steels in aqueous solutions and hydrogen-containing gaseous environments (Kerns et al., 1977; Marsh and Gerberich, 1992). In these systems, HE is broadly described as a three-step process. Firstly, hydrogen is introduced into the metal, via electrochemical charging (e.g., as in cathodically polarized samples in aqueous media) or via gaseous absorption. In some cases, hydrogen may be introduced in the lattice prior to stressing, e.g., during fabrication. This situation is commonly referred to as internal hydrogen embrittlement (IHE). Secondly, atomic hydrogen is transported through the metal lattice, increasing its concentration in the tensile-stressed surroundings of the crack tip due to gradients in the chemical-potential (Völkl and Alefeld, 1978; Fukai, 1993). In the absence of a crack, atomic hydrogen may be transported to an initiation location. Thirdly, the combined action of stress and hydrogen concentration leads to failure of the metal in an embrittled zone.

The introduction of hydrogen into the metal (step 1) in turn comprises a sequence of phenomena, namely transport of hydrogen within the environment, dissociative adsorption or proton deposition at the surface to produce adsorbed hydrogen atoms, and absorption into the bulk metal lattice. Absorption may occur all along the length of the crack, and the continuously evolving state of the crack flanks influences the process. To the best of our knowledge, no complete calculations, including the environment, surface, and bulk metal regions have been performed to date. An alternative approach is to assume that hydrogen absorption can be described via appropriate boundary conditions (e.g., Sofronis and McMeeking, 1989). In principle, these boundary conditions may be related to transport in the crack environment and reactions at the crack surfaces (Turnbull et al., 1996; Turnbull, 2001), but this connection is not well established at present.

Atomic hydrogen, being the smallest possible impurity, is generally considered to be transported by interstitial diffusion (step 2). First-principles calculations of H atom diffusion in Fe (Jiang and Carter, 2004a) confirm that this diffusion pathway results

in kinetic constants consistent with measured values. The driving force for diffusion is the gradient of the chemical potential, which is sensitive to stress gradients (Völkl and Alefeld, 1978; Fukai, 1993). Several additional factors, including plastic deformation, trapping and microstructure, influence hydrogen diffusion and jointly result in an effective diffusion constant (Oriani, 1970).

The precise mechanism by which hydrogen embrittles metals (step 3) has been the subject of considerable conjecture (e.g., Birnbaum, 1990, and references therein). Some of the proposed mechanisms are: (i) hydrogen-induced phase changes (Westlake, 1969; Nelson, 1976; Oriani, 1990); (ii) hydrogen-enhanced localized plasticity (HELP) (Beachem, 1972; Birnbaum and Sofronis, 1994); and (iii) hydrogen-reduced cohesive energy (Troiano, 1960; Oriani, 1972; Oriani and Josephic, 1977).

In this paper, we present a model of hydrogen embrittlement based upon: (i) a cohesive law dependent on impurity coverage that is calculated from first principles; (ii) a stress-assisted diffusion equation with appropriate boundary conditions accounting for the environment; (iii) a static continuum analysis of crack growth including plasticity; and (iv) the Langmuir relation determining the impurity coverage from its bulk concentration. The model builds on preliminary work of Nguyen, 2000, and is described in detail in Section 2. Previous related models include those in van Leeuwen (1975), Doig and Jones (1977), Gerberich et al. (1988), Lee and Unger (1988), and Unger (1989). In the present work, the reduction in cohesive energy due to hydrogen is deduced from first-principles calculations of decohesion by van der Ven and Ceder (2003) and Jiang and Carter (2004b). In addition, renormalization group ideas developed by Nguyen and Ortiz (2002), and Hayes et al. (2004), are used in order to scale the atomic-level cohesive properties up to the continuum scale. The renormalized cohesive law is then embedded into cohesive elements (Ortiz and Pandolfi, 1999) for use in large-scale calculations.

By way of validation of the model, in Section 3 we consider the effect of the following parameters: yield strength, stress intensity factor, hydrogen concentration in the environment, and temperature. The calculations reproduce the following experimental trends: (i) time to initiation and its dependence on yield strength and stress intensity factor; (ii) finite crack jump at initiation; (iii) intermittent crack growth; (iv) stages I and II of crack growth and their dependence on yield strength; (v) the effect of the environmental impurity concentration on the threshold stress intensity factor; and (vi) the effect of temperature on stage II crack velocity in the low-temperature range. In addition, the theoretically and experimentally observed intermittent cracking may be understood as being due to a time lag in the diffusion of hydrogen towards the cohesive zone, since a buildup of hydrogen is necessary in order for the crack to advance. The predictions of the model are in good quantitative agreement with available measurements, suggesting that hydrogen-induced degradation of cohesion is a likely mechanism for HE and SCC of high-strength steels.

In Section 4 we summarize and draw the main conclusions of the work.

2. Formulation of the model

2.1. Cohesive laws accounting for impurity segregation

The centerpiece of the present approach is a cohesive model of fracture which accounts for the effect of impurity segregation. Cohesive theories of fracture, pioneered by Dugdale (1960), Barenblatt (1962), Rice (1968) and others, regard fracture as a gradual phenomenon in which separation takes place across an extended crack 'tip', or cohesive zone, and is resisted by cohesive tractions. An appealing feature of this approach is that it does not presuppose a particular type of constitutive response in the bulk of the material, the extent of crack growth, or the size of the plastic zone. In addition, the location of successive crack fronts is itself an outcome of the calculations.

The effect of impurities such as hydrogen on cohesive laws in metals cannot be elucidated classically but requires a full quantum-mechanical treatment of this very localized and complex event. Thus, for instance, van der Ven and Ceder (2003) used density functional theory (DFT) to obtain a complete set of traction-separation curves for rigid Al(1 1 1) surfaces with hydrogen coverages between 0 and 1 monolayers (ML), the latter representing an interface with a surface concentration equal to the saturation value. Jiang and Carter (2004b) similarly used DFT to investigate the decohesion of bcc Fe(1 1 0) surfaces with varying hydrogen coverage.

The integration of cohesive laws determined from first principles into macroscopic engineering calculations entails some difficulty. The first-principles interplanar potentials are characterized by peak stresses of the order of the theoretical strength of the crystal. In addition, the crystal loses its bearing capacity after an interplanar separation of only a few angstroms. The cohesive-zone sizes attendant to first-principles interplanar potentials are also on the nanometer scale. Camacho and Ortiz (1996) determined that finite-element solutions of cohesive fracture exhibit strong convergence only when the mesh resolves the cohesive-zone size. Therefore, finite-element calculations based on first-principles interplanar potentials must provide full atomistic resolution in the vicinity of the crack tip, which is both unfeasible and impractical.

Nguyen and Ortiz (2002) proposed a renormalization procedure which addresses the disconnect between atomistic and engineering cohesive descriptions. The renormalization procedure has been extended and verified by Hayes et al. (2004). Consider a thin dislocation-free strip of elastic material inside which a crack propagates, with the material outside described by continuum plasticity. For instance, the width of the strip may be taken to be comparable to the dislocation spacing or the dislocation cell size (Tvergaard, 1997, 1998). The dislocation-free strip contains a large but finite number N of atomic planes whose separation is governed by an atomic-level cohesive, or traction-separation, law. Nguyen and Ortiz (2002), and Hayes et al. (2004), have shown that, for a large N, the collective behavior of the atomic plane ensemble in the strip is governed by the simple *universal* law

$$\bar{\sigma}(\bar{\delta}) = \begin{cases} \bar{\sigma}_c(1 - \bar{\delta}/\bar{\delta}_c) & \text{if } \bar{\delta} < \bar{\delta}_c, \\ 0 & \text{otherwise,} \end{cases} \tag{1}$$

where $\bar{\delta}$ is the total opening displacement of the strip, $\bar{\delta}_c$ is the effective critical opening displacement of the strip, and $\bar{\sigma}_c$ the corresponding peak or critical stress. Thus, the renormalized traction-separation law is rigid up to a critical stress $\bar{\sigma}_c$, and subsequently drops linearly and reduces to zero upon the attainment of a critical $\bar{\delta}_c$. In addition, $\bar{\sigma}_c$ and $\bar{\delta}_c$ scale with N as

$$\bar{\sigma}_c = 2\sqrt{\frac{A\gamma_r}{N}}, \tag{2a}$$

$$\bar{\delta}_c = 2\sqrt{\frac{\gamma_r N}{A}}, \tag{2b}$$

where γ_r is the energy of the structurally *relaxed* surface and A is the elastic modulus of a single pair of atomic planes in uniaxial strain. The corresponding cohesive zone size L_{coh} scales as N, since $L_{coh} \sim 1/\bar{\sigma}_c^2$. Thus, for large N, the effective behavior of the atomic planes ensemble is characterized by a critical stress much smaller, and an opening displacement and a cohesive zone size much larger, than the corresponding atomic-level values. The foregoing results are rigorous asymptotically as $N \to \infty$, but as Hayes et al. (2004) have shown by first principles calculations for several materials, a slab with a thickness of ≈ 10 atomic layers gives an effective cohesive law with a shape almost equal to the renormalized. Therefore, the number of planes does not need to be very large. The renormalization procedure just described greatly reduces the spatial resolution requirements on the engineering model.

Suppose, for definiteness, that the atomic level interplanar traction-separation relation is well approximated by the UBER form (Rose et al., 1984)

$$\sigma = A\delta e^{-\delta/\delta_c}, \tag{3}$$

where δ_c is the critical separation at which σ attains its maximum value

$$\sigma_c = e^{-1} A\delta_c. \tag{4}$$

In addition,

$$2\gamma = e\sigma_c\delta_c. \tag{5}$$

The calculations of van der Ven and Ceder (2003) show that, for H in Al(1 1 1), δ_c is insensitive to coverage throughout the range $0 \leqslant \theta \leqslant 1$ and, accordingly, we take it to be constant in the case of Fe(1 1 0) as a first approximation. By contrast, the cohesive strength σ_c depends sensitively on coverage. A fit to the data of Jiang and Carter (2004b) for the H/Fe system, Fig. 1(a), gives

$$\gamma(\theta) = (1 - 1.0467\theta + 0.1687\theta^2)\gamma(0), \tag{6}$$

where $\theta = \Gamma/\Gamma_s$ is the coverage, Γ is the surface hydrogen concentration and Γ_s is its saturation value. Other first principles calculations of the effect of hydrogen on cohesion have been carried out by Zhong et al. (2000). They considered a Fe $\Sigma 3[1\,\bar{1}\,0](1\,1\,1)$ grain boundary and the corresponding H/Fe(1 1 1) surface, with a partial coverage ($\theta < 1$) of the decohering interface. These differences preclude a detailed comparison, although we expect that, overall, our high coverages and our use of the most stable free surface Fe(1 1 0) deliver a stronger embrittlement.

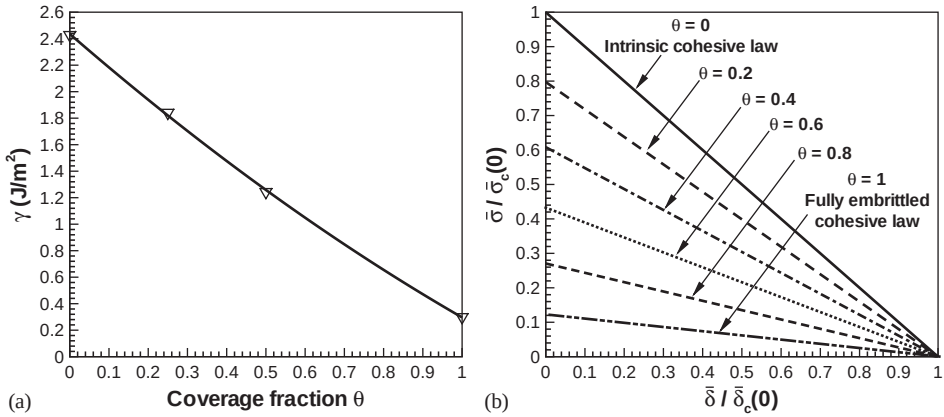

Fig. 1. Dependence of cohesive energy on hydrogen coverage of a decohering bcc Fe(1 1 0) interface, calculated by first principles. (a) Effect of hydrogen on cohesive energy of bcc Fe(1 1 0) (Jiang and Carter, 2004b) calculated by first principles. Symbols: calculated; line: fit. (b) Effect of hydrogen coverage θ on renormalized and elastically corrected cohesive laws for bcc Fe(1 1 0).

Allowing (4) and (5) to take on a coverage dependence and inserting them into (2a) and (2b), taking $\gamma = \gamma_r$ for simplicity, we obtain

$$\bar{\sigma}_c(\theta) = 2eN^{-1/2}\sigma_c(\theta), \tag{7a}$$

$$\bar{\delta}_c = 2N^{1/2}\delta_c. \tag{7b}$$

As is evident from (7a) and (7b), the coverage dependence of the atomic-level peak stress σ_c is transferred to the effective cohesive strength $\bar{\sigma}_c$ upon renormalization. In addition, the effective critical opening displacement $\bar{\delta}_c$ retains the coverage independence of δ_c upon renormalization.

The preceding developments result in the impurity-dependent effective cohesive law shown in Fig. 1(b). In particular, it follows from (7a), (5) and (6) that

$$\frac{\bar{\sigma}_c(\theta)}{\bar{\sigma}_c(0)} = \frac{\sigma_c(\theta)}{\sigma_c(0)} = 1 - 1.0467\theta + 0.1687\theta^2, \tag{8}$$

which, in conjunction with the constancy of $\bar{\delta}_c$, fully determines the dependence of the effective cohesive law, Eq. (1), on coverage. However, it is worth noting that, for elastic–plastic materials cracking along a cohesive interface, the shape of the cohesive law has been shown to have a minor effect on the fracture properties of the interface (Tvergaard and Hutchinson, 1992).

2.2. Stress-assisted impurity diffusion

Next we address the mechanisms by which hydrogen is transported to the crack tip, namely, absorption at the boundary, bulk diffusion and segregation of hydrogen to the cohesive zone. Consideration of these mechanisms leads to the formulation of a

stress-assisted diffusion problem. We are specifically concerned with the diffusion of impurities in a metal containing cracks in contact with an aggressive environment.

We consider the impurity/host metal system to be a dilute ideal solution. The impurities in the lattice are modelled as point defects causing dilatational distortion only, therefore interacting with the stress field $\boldsymbol{\sigma}$ only through the hydrostatic stress $p = \mathrm{Tr}(\boldsymbol{\sigma})/3$, which is taken to be positive for tensile stresses. The molar bulk chemical potential of the impurity can then be written as

$$\mu = \mu_0(T) + RT \ln C - pV_{\mathrm{H}}, \tag{9}$$

where C is the impurity mole fraction, $R = 8.314$ J/mol K is the universal gas constant, T is the absolute temperature, and V_{H} is the partial molar volume of the impurity in solid solution. μ_0 is the bulk chemical potential at $p = 0$ and $C = 1$. Throughout this work, we take the temperature to be constant and V_{H} to be independent of C and $\boldsymbol{\sigma}$.

The flux of hydrogen $\mathbf{J}$ is related to the chemical potential by Fick's law, namely (Porter and Easterling, 1981)

$$\mathbf{J} = -MC\nabla\mu, \tag{10}$$

where M is the impurity mobility. Inserting (9) into (10) we obtain

$$-\mathbf{J} = D\nabla C - \frac{DV_{\mathrm{H}}}{RT} C\nabla p, \tag{11}$$

where $D = MRT$ is the bulk diffusivity. In addition, the conservation equation for the impurity is

$$-\nabla \cdot \mathbf{J} = \frac{\partial C}{\partial t}. \tag{12}$$

Inserting (11) into (12) we obtain the diffusion equation

$$\frac{\partial C}{\partial t} = D\nabla^2 C - \frac{DV_{\mathrm{H}}}{RT} \nabla C \cdot \nabla p - \frac{DV_{\mathrm{H}}}{RT} C\nabla^2 p, \tag{13}$$

which must be satisfied in the interior B of the body.

For purposes of formulating appropriate boundary conditions three main regions of the boundary may be identified: (i) the exterior surface of the body; (ii) the crack flanks, and (iii) the cohesive zones at the tip of the cracks. We shall assume that the conditions at the external boundary may be mathematically represented by a standard Dirichlet boundary condition, consisting of prescribing the concentration, set here at $C = 0$. This choice of boundary condition leads to no hydrogen entering into the system through remote boundaries. The choice of remote boundary conditions may be expected to have a minor effect on the conditions near the crack tip. In addition, we shall assume that the crack flanks are in equilibrium with the environment, i.e.,

$$\mu = \mu_{\mathrm{env}}, \tag{14}$$

which, upon insertion of (9), becomes

$$C = C_{\mathrm{eq}}(p) = C_{\mathrm{eq}}(0)\mathrm{e}^{pV_{\mathrm{H}}/RT}, \tag{15}$$

where $C_{\mathrm{eq}}(p)$ is the equilibrium bulk concentration at the crack flanks at hydrostatic stress p and $C_{\mathrm{eq}}(0)$ is the equilibrium bulk concentration at zero hydrostatic stress. In

aqueous environments, μ_{env} may vary along the crack flanks. For instance, hydrolysis of highly concentrated metal ions generates a localized acidified medium (Galvele, 1981; Turnbull, 2001), giving an enhanced source of hydrogen. However, Sharland and Tasker (1988) have shown that such variations are negligible up to very small distances from the crack mouth, and that μ_{env} may be taken to be uniform to a good approximation. For want of a better model, in the calculations presented here we simply assume a zero normal flux boundary condition

$$J_n = \mathbf{J} \cdot \mathbf{n} = 0 \tag{16}$$

over the cohesive zones at crack tips. In this equation, $\mathbf{n}$ denotes the outward unit vector normal to the boundary. In addition, we assume initial boundary conditions of the form

$$C = \begin{cases} C_{\text{eq}}(p), & \text{on crack flanks,} \\ 0, & \text{elsewhere} \end{cases} \tag{17}$$

corresponding to a sudden exposure of an otherwise impurity-free metal to an aggressive environment, followed by the establishment of an instantaneous equilibrium between environment-crack flanks.

It should be carefully noted that the conditions prevailing in the environment immediately adjacent to crack tips are complex and do not appear to be entirely understood at present. For instance, Lu et al. (1981) found evidence suggesting that for 4340 steel strained in gaseous H_2S, at 0.133 kPa and below room temperature, the crack propagation rate was controlled by transport in the gas phase, an indication that the small openings near the crack tip have the effect of hindering transport. More complex yet are the conditions present in aqueous environments due to the localized acidification mentioned above. Continuously strained material at crack tips presents an additional complexity.

The boundary conditions utilized in models or simulations of hydrogen embrittlement variously include Dirichlet, or prescribed concentration, boundary conditions (Taha and Sofronis, 2001); Neumann, or prescribed flux, boundary conditions (Sofronis and McMeeking, 1989; Taha and Sofronis, 2001; Turnbull et al., 1996); and mixed Dirichlet–Neumann boundary conditions (Nguyen, 2000), consisting of prescribing a linear combination of concentration and normal flux. In this latter case, the coefficients of the linear combination may be made to depend on the crack opening so as to achieve a continuous transition between a zero flux boundary condition at the cohesive zone vertex, where crack opening vanishes, and the Dirichlet condition (15) at the start of the traction-free crack flanks (Nguyen, 2000). Taha and Sofronis (2001) compared the transient solutions obtained by the use of Dirichlet and Neumann boundary conditions and found the effects to be significant in some cases. In a different study, Turnbull et al. (1996) found that when flux boundary conditions are enforced along the entire length of the crack, but with a higher flux or current density near the crack tip, the bulk material surrounding the crack tip acts as a sink, resulting in a steady-state concentration at the crack tip lower than that corresponding to concentration boundary conditions. Based on their study Turnbull et al. advocated the use of flux boundary conditions, especially in materials with high hydrogen diffusivity. It also has been noted

that bulk charging may be dominant under certain conditions (Turnbull and Saenz de Santa Maria, 1988), and in such cases the boundary conditions surrounding the crack tip may be unimportant.

In order to couple the diffusion problem to the impurity-dependent cohesive law described in the preceding section, the bulk concentration C must be related to the surface concentration Γ in the cohesive zone. This connection is supplied by the Langmuir–McLean isotherm (Hondros and Seah, 1977)

$$\theta = \frac{C}{C + \exp(-\Delta g_{\mathrm{b}}^{0}/RT)}, \tag{18}$$

where $\Delta g_{\mathrm{b}}^{0}$ is the free energy difference between the adsorbed and bulk standard states.

2.3. Coupling of diffusion and mechanics

The preceding developments define a *coupled* transient diffusion-mechanics problem. The diffusion problem governs the transport of hydrogen to the crack tip, whereas the mechanics problem accounts for the plasticity and fracture of the specimen. Specifically, the stress-assisted diffusion is governed by (13) and its associated boundary and initial conditions. The evolution of the crack is governed by the impurity-dependent cohesive law presented in Section 2.1, subject to the Langmuir–McLean isotherm. The plasticity of the material is accounted for by means of a standard small-strain continuum plasticity model with power-law strain hardening (e.g., Nguyen et al., 2001). Due to the slow nature of corrosion cracking, plastic deformations are taken to be rate-independent and the mechanics problem is solved statically.

The coupling between the diffusion and mechanics problems takes place in two ways. First, diffusion affects the mechanical properties via hydrogen buildup over the cohesive zone, as indicated by Eqs. (18) and (8), which decreases the fracture toughness of the material. Second, mechanics affects the diffusion rate via the stress field, which appears in the pressure dependence of the bulk chemical potential, Eq. (9).

3. Comparison between calculations and experiments

The specific test configuration considered is the center-crack panel geometry shown in Fig. 2. The specimen is loaded by means of a constant and uniform tensile stress σ normal to the plane of the crack. In calculations, the specimen is discretized into six-node triangular finite elements. Due to the symmetry of the problem, the computational domain can be restricted to the upper right quarter of the specimen. The computational mesh is graded so as to resolve the renormalized cohesive zone size along the crack plane at all stages of growth of the crack. The cohesive law is integrated into the calculations by means of six-node cohesive elements (Ortiz and Pandolfi, 1999). We advance the solution in time by means of a standard staggered procedure (e.g., Park and Felippa, 1983), consisting of alternating the solution of a diffusion problem and a quasistatic fracture and plasticity problem.

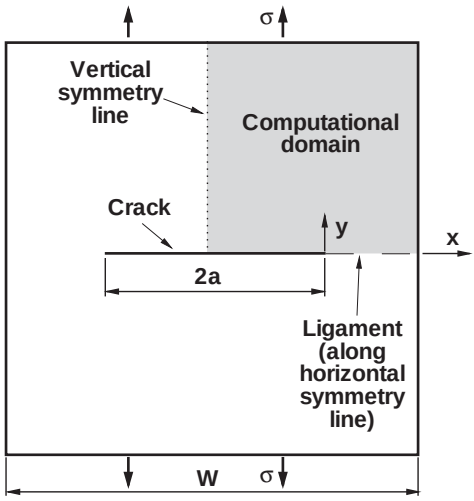

Fig. 2. Upper left quarter of the center-cracked panel used in the calculations, showing the origin of coordinates, the vertical and horizontal symmetry lines. A uniform remote stress σ is applied.

The material system chosen for analysis concerns a series of quenched and tempered AISI 4340 high-strength steels in aqueous solutions. The behavior of this system is known to depend sensitively on heat treatment, characterized mainly by the tensile yield strength σ_{y0} at room temperature, and on testing temperature (Marsh and Gerberich, 1992). The elastic properties are characterized by Young's modulus $E = 207$ GPa (Sofronis and McMeeking, 1989) and Poisson's ratio $\nu = 0.3$ (Sofronis and McMeeking, 1989). The strain-hardening inverse exponent n varies with thermal treatment. In calculations, we use the linear fit

$$n = A\sigma_{y0} + B, \tag{19}$$

with $A = 0.01845\ \mathrm{MPa}^{-1}$ and $B = -6.59617$, to experiments carried out by Larson and Nunes (1962) in the range $\sigma_{y0} = 750 - 1800$ MPa. The assumed dependence of the fracture toughness K_C on σ_{y0} is tabulated in Table 1, which roughly bisects the experimental data band reported by Sandoz (1972). The fracture energy is then computed by means of the relation

$$G_C = \frac{K_C^2}{E/(1-\nu^2)}. \tag{20}$$

Following the analysis of Tvergaard and Hutchinson (1992), we set the effective cohesive strength $\bar{\sigma}_c = 4\sigma_{y0}$, and compute the effective critical opening $\bar{\delta}_c$ displacement from the relation

$$G_C = \tfrac{1}{2}\,\bar{\sigma}_c\bar{\delta}_c. \tag{21}$$

This fracture energy G_C is higher than 2γ as used in Section 2.1, and we assume the same embrittlement factor for G_C as given in Eqs. (6) and (8), with the implication that

Table 1
Room temperature mechanical properties for AISI 4340 steels with varying tensile yield strengths σ_{y0}. n is the inverse strain hardening exponent in Eq. (19), K_C is the fracture toughness in Eq. (20), and q is the thermal softening exponent in Eq. (24)

AISI 4340 mechanical properties				
σ_{y0} (MPa)	1000	1200	1400	1600
n	11.9	15.5	19.3	23.0
K_C (MPa $\sqrt{\text{m}}$)	120	100	75	52
q	0.55	0.46	0.39	0.35

Table 2
Hydrogen related material properties for AISI 4340 steel. D_{eff} is the effective diffusion coefficient (see text), V_H (Sofronis and McMeeking, 1989) is the molar volume of solution of H in Fe, Δg_b^0 is the trapping energy of H at Fe grain boundaries, and Γ_s (Wang and Vehoff, 1991) is the density of surface sites in Fe for adsorption of H

Hydrogen-related material parameters			
D_{eff} (m^2/s)	V_H (m^3/mol)	Δg_b^0 (kJ/mol)	Γ_s (mol/m^2)
10^{-10}	2.0×10^{-6}	30	2.65×10^{-5}

the effect of hydrogen on cohesion also causes the plastic dissipation due to dislocation activity close to the interface to decrease. This "valve-like" effect of 2γ on G_C has been recognized earlier (Jokl et al., 1980; Rice and Wang, 1989; Beltz et al., 1996; Suo et al., 1993).

The properties related to the diffusion problem are collected in Table 2. In particular, the effect of trapping (Oriani, 1970) is accounted for by means of an effective diffusivity D_{eff}. The value of D_{eff} used in calculations is consistent with reported values (Scully and Moran, 1988; Pound, 1998). The free energy of adsorption from the bulk to a grain boundary is characterized in terms of the trapping energy Δg_b^0, for which we choose a value within the range of variation of the reported data (Hirth, 1980; Gao and Wei, 1985; Gerberich et al., 1988). Unless otherwise stated, the concentration $C_{eq}(0)$ used in simulations is $5.5 \times 10^{-6} = 1$ wt ppm, which, according to Gangloff (1986), corresponds to a 3% NaCl aqueous solution.

We now proceed to explore the range of behaviors predicted by the model—and to assess its fidelity—by way of comparison with experimental data. A typical fracture mechanics curve under mode I monotonic loading is schematically shown in Fig. 3. The salient features of this curve are: the threshold stress intensity factor K_{SCC}, which signals the onset of the steeply rising part of the curve known as *stage* I; the plateau, or *stage* II characterized by a nearly K-independent velocity $V_{P,II}$; and the limit value K_C at which pure mechanical failure occurs. In keeping with these observations, we specifically test the ability of the model to predict threshold values, effect of environment concentration, crack-growth curves, and other properties.

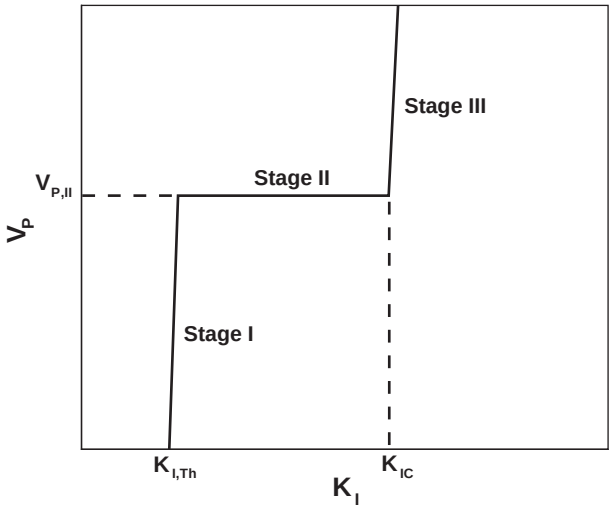

Fig. 3. Fracture mechanics curve characteristic of environment assisted cracking, giving the crack propagation rate V_P versus applied stress intensity factor K_I. The threshold $K_{I,th}$ may be named according to the relevant phenomenon, i.e., K_{SCC}, K_H, etc.

3.1. Room temperature results

Fig. 4 displays a typical crack growth curve from our simulations. An incubation time exists during which hydrogen builds up around the crack tip. During this incubation time the crack vertex (at x_v), i.e., the point at which the opening displacement vanishes, advances while the trailing point (at x_f) at which the tractions vanish remains ostensibly stationary. This in turn results in the elongation of the cohesive zone size $L_{coh}=x_v-x_f$. Since L_{coh} scales as $\bar{\sigma}_c^{-2}$ for constant cohesive stress (e.g., Rice, 1968), the elongation of L_{coh} is expected in view of the reduction of $\bar{\sigma}_c$ caused by the hydrogen build-up. When the embrittlement is sufficient (in this case, at $t_i = 795$ s), the crack jumps a distance Δa_i of the order of 100 μm. Similar values for the initial crack jump length, Δa_i, have been found experimentally for notched specimens under external hydrogen (Hirose and Mura, 1984b; Page and Gerberich, 1982).

Remarkably, crack propagation is predicted to take place *intermittently*, as a succession of quiescent periods punctuated by discrete jumps. Intermittent crack growth has been observed experimentally for compact tension samples of AISI 4340 steel in 0.1 N H_2SO_4 (Hirose and Mura, 1984a), where crack jumps of 7–40 μm were recorded during crack evolution. Gao et al. (1984) also found finger-like protrusions of crack fronts, about 20 to 80 μm deep, in a precracked sample of AISI 4340 steel in H_2S which may be indicative of the size of propagation jump events. We verify that the crack jumps are not artifacts of the spatial or time discretization imposed, since the jump lengths span several internodal spacings, and the time periods when the crack is at rest between jump events (encircled in Fig. 4) comprise several time steps.

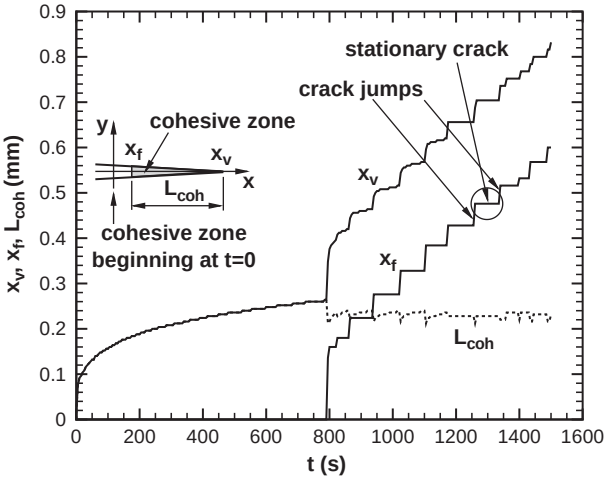

Fig. 4. Calculated crack advancement as a function of time. Note the crack jumps at initiation and during propagation, along with an almost constant cohesive zone length $L_{coh} = x_v - x_f$. x_f locates the traction-free point, behind which the crack flanks experience zero traction. x_v locates the vertex of the cohesive zone, ahead of which there is zero opening displacement. At $t=0$ and before initial mechanical loading, $x_v = x_f = 0$, while at times prior to crack initiation, x_v advances and x_f remains at zero. $\sigma_{y0}=1400$ MPa, $K=50$ MPa $\sqrt{m}$, $C_{eq}(0) = 5.5 \times 10^{-6}$.

During crack propagation the curves for x_v and x_f are essentially parallel and L_{coh} remains nearly constant. An average steady state is eventually attained, and crack jumps $\Delta a_p \approx 40$ μm, smaller than the jump at initiation, are predicted, in keeping with experimental observation (Hirose and Mura, 1984a).

The remarkable embrittlement displayed by this system is consistent with recent first principles calculations by Jiang and Carter (2004a) which show that hydrogen both thermodynamically and kinetically prefers to aggregate to surfaces rather than remain in bulk Fe. This suggests that while the equilibrium bulk concentration of hydrogen is very low, as soon as a surface starts to form, H rapidly flows to it, and coverages of $\theta = 1$ can indeed be attained due to nearly negligible repulsions between hydrogen atoms on the surface.

Fig. 5 shows that the model also captures the expected dependence of initiation time on stress intensity factor and yield strength, when compared to data available from experiments on notched samples. As the yield strength increases, the time to initiation decreases, due to the decrease in intrinsic fracture toughness. Likewise, as the stress intensity factor increases, the time to initiation decreases due to the faster transport of hydrogen to the crack tip.

Examination of the stress, deformation, and concentration fields immediately before and after crack initiation reveals much about the initiation mechanism. Fig. 6 displays the interface concentration Γ along the cohesive zone, right before and after several evenly spaced time steps. Also shown are two bulk concentrations along the cohesive zone, the equilibrium value C_{eq} as given by Eq. (15), and the actual values of C,

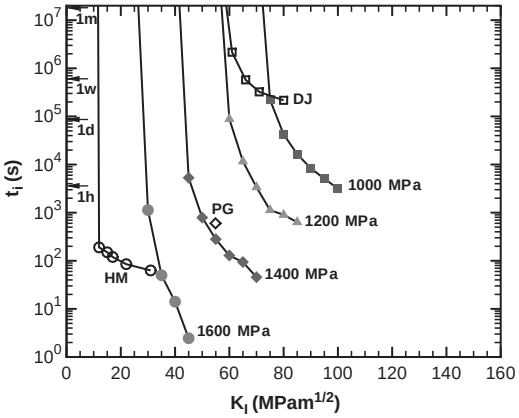

Fig. 5. Calculated crack initiation times for AISI 4340 steels. Filled symbols: calculated, $C_{eq}(0)=5.5\times10^{-6}$; open symbols: experimental (notches); PG: 1314 MPa, notch 0.21 mm (Page and Gerberich, 1982); HM: 1530 MPa, notch 0.11 mm (Hirose and Mura, 1984b); DJ: Austenitic 1000 MPa, notch 0.8 mm (Doig and Jones, 1977).

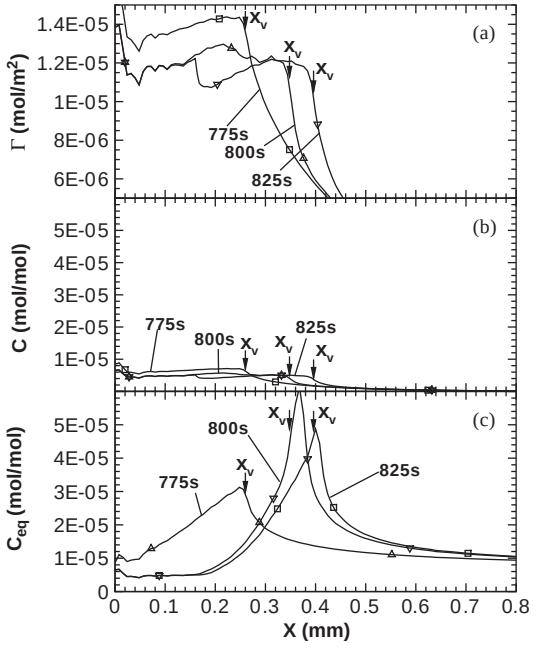

Fig. 6. Hydrogen concentrations along the crack line: (a) Γ (at the interface), (b) C (actual bulk concentration), and (c) C_{eq} (equilibrium bulk concentration), slightly before (at $t_1 = 775$ s) and right after (at $t_2 = 800$ s) crack initiation, and slightly later (at $t_3 = 825$ s). Arrows indicate x_v for each time. The saturation concentration is $\Gamma^s = 2.65 \times 10^{-5}$ mol/m^2. $X = 0$ is the initial location of x_v and x_f. $\sigma_{y0} = 1400$ MPa, $K = 50$ MPa $\sqrt{m}$, $C_{eq}(0) = 5.5 \times 10^{-6}$.

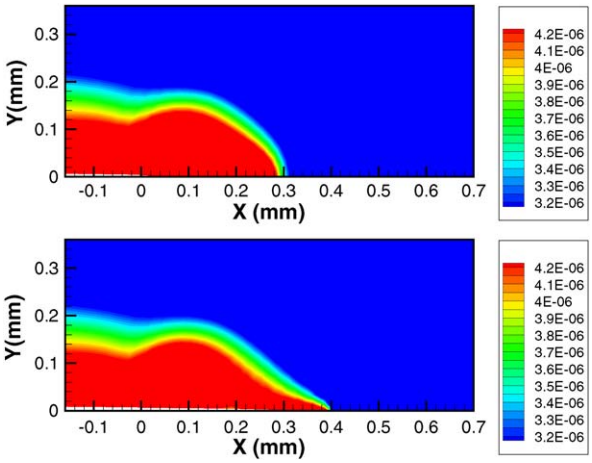

Fig. 7. Hydrogen concentration contours before (at $t_1 = 775$ s) and after (at $t_3 = 825$ s) crack initiation. $\sigma_{y0} = 1400$ MPa, $K = 50$ MPa $\sqrt{\text{m}}$, $C_{eq}(0) = 5.5 \times 10^{-6}$.

given by Eq. (13), which are in turn equilibrated with Γ via Eq. (18). Slightly before initiation (at $t_1 = 775$ s), Γ builds up near the location of the peak in hydrostatic stress x_{pp}, which coincides with the peak in C_{eq} and is closer to x_v than to x_f. However, the actual concentration C at x_{pp} is five times lower than C_{eq} even though the applied K is 50 MPa $\sqrt{\text{m}}$, only slightly above threshold. As we will see, the actual concentration C remains much lower than C_{eq} during propagation as well. Thus, once the K_{SCC} threshold is exceeded, the critical embrittling concentration is a small fraction of the equilibrium concentration. By contrast, below K_{SCC}, the concentration attains the value C_{eq} everywhere, yet no cracking occurs.

After initiation, hydrogen peaks in Γ and C that shift with crack propagation begin to form. Fig. 7 displays two snapshots of hydrogen concentration (C) contours, before and after crack initiation. Some hydrogen accumulates at approximately 0.15 mm above and ahead of x_f due to a pocket of plastic strain, but this hydrogen has no effect on crack propagation, as discussed below. After the crack has initiated, a hydrogen peak begins to form at $X \approx 0.38$ mm, ahead of the previous peak location and close to x_v. The new peak can also be seen in Fig. 6(b). It is this peak that traverses the sample along with the crack.

The microscopic quantities follow the intermittent growth of the crack much in the same way as for the initiation step, but in an average steady state. Fig. 8 illustrates this behavior, where Γ, C_{eq} and C are shown right before a jump (at $t_4 = 1250$ s), while the crack remains still ($t = 1265 - 1335$ s), and after the next jump (at $t_7 = 1350$ s), corresponding to the region encircled in Fig. 4. The most important changes occur precisely during the bursts at steps 1255–1265 and 1335–1340 s, when the Γ profile advances and at the same time decreases in the peak region. This is due to the shift in C_{eq} profile, which mimics that of p, since hydrogen is transported from the region in the left shoulder of the C_{eq} peak at 1250 s to the region in the right shoulder. After this

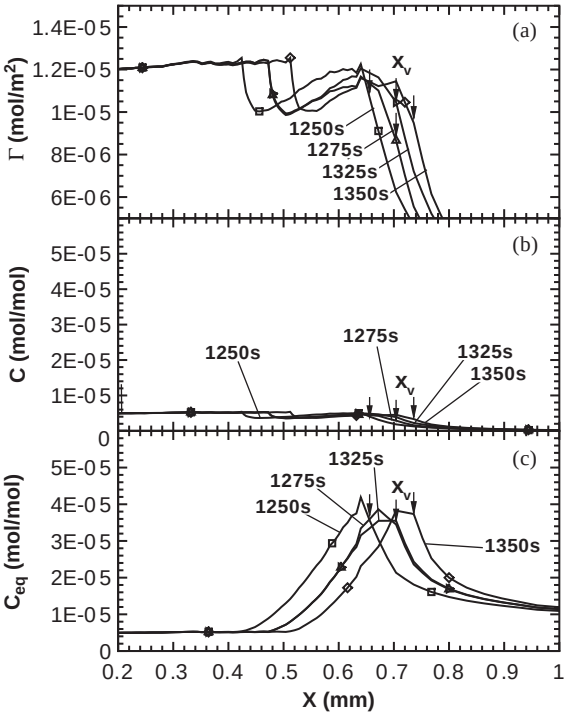

Fig. 8. Hydrogen concentrations along the crack line: (a) Γ (at the interface), (b) C (actual bulk concentration), and (c) C_{eq} (equilibrium bulk concentration), right before (at $t_4 = 1250$ s) and slightly after (at $t_5 = 1275$ s) a crack propagation jump, and slightly before (at $t_6 = 1325$ s) and slightly after (at $t_7 = 1350$ s) the next crack jump. The time spanned corresponds to the circle in Fig. 4. Arrows indicate x_v for each time. The saturation concentration is $\Gamma^s = 2.65 \times 10^{-5}$ mol/m^2. $X = 0$ is the initial location of x_v and x_f. $\sigma_{y0} = 1400$ MPa, $K = 50$ MPa $\sqrt{\text{m}}$, $C_{eq}(0) = 5.5 \times 10^{-6}$.

initial decrease, during the period 1265–1335 s of crack stationarity, the concentration increases again around the new peak, until a new burst sets in. Comparing the Γ, C_{eq} and C profiles before the two jumps, at 1250 and 1325 s, it can be seen that they are similar but translated one from another by the size of the jump, 48 μm. The same relation holds for the Γ profiles after the jumps, confirming that the intermittent crack growth process repeats has a cyclic character.

Fig. 9 illustrates the hydrogen concentration contours before and after the crack jumps. The pocket of hydrogen shown in Fig. 7 has a slightly decreased concentration due to outward hydrogen diffusion. More importantly, the hydrogen peak shifts by the crack jump distance to the right of the figure, as is also evident in Fig. 8.

Fig. 10 displays the wake of plastic strain trailing the crack. The wake structure clearly reflects the discontinuous nature of the crack growth, and the jump spacing is clearly apparent. The pocket of plastic strain mentioned in connection to Fig. 7 does not affect the crack propagation rate, since it remains almost constant (Fig. 4) as

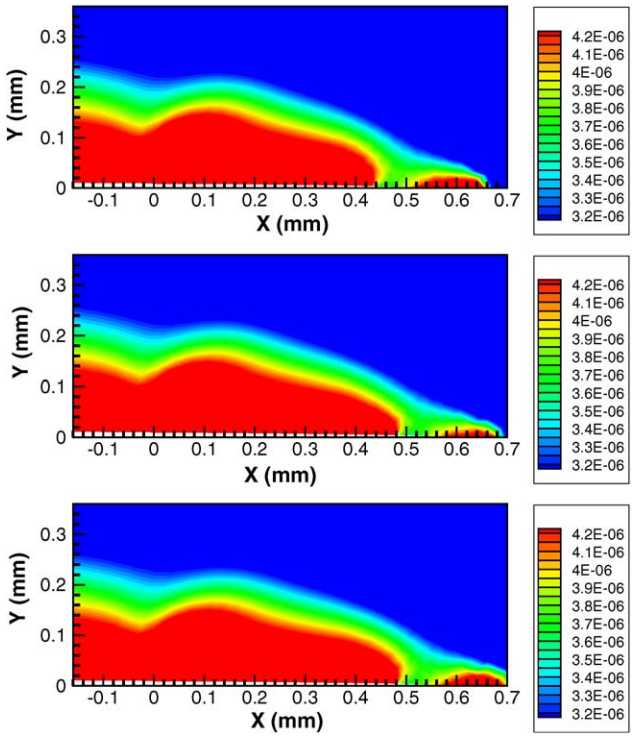

Fig. 9. Hydrogen concentration contours before (at $t_4 = 1250$ s) and after (at $t_5 = 1275$ s) a crack jump, and before (at $t_6 = 1325$ s) the following jump. $\sigma_{y0} = 1400$ MPa, $K = 50$ MPa $\sqrt{\text{m}}$, $C_{eq}(0) = 5.5 \times 10^{-6}$.

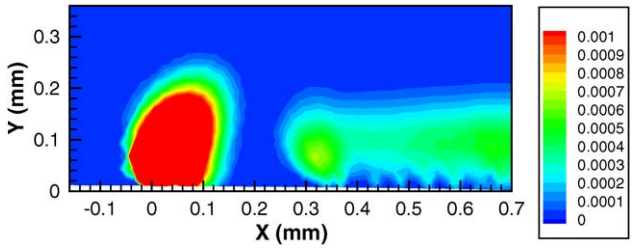

Fig. 10. Contour levels of plastic strain after the crack has traversed the region shown. There is a pocket of plastic strain at the initial location of the cohesive zone, and the discontinuous crack advancement can be seen in the plastic wake. $\sigma_{y0} = 1400$ MPa, $K = 50$ MPa $\sqrt{\text{m}}$, $C_{eq}(0) = 5.5 \times 10^{-6}$.

the crack zone moves away from the pocket. Therefore, the main source of hydrogen involved in the growth process does not originate in the pocket.

The calculated $V_P - K$ curves are shown in Fig. 11, along with several experimentally determined curves for AISI 4340 in aqueous solutions (Hirose and Mura, 1984a;

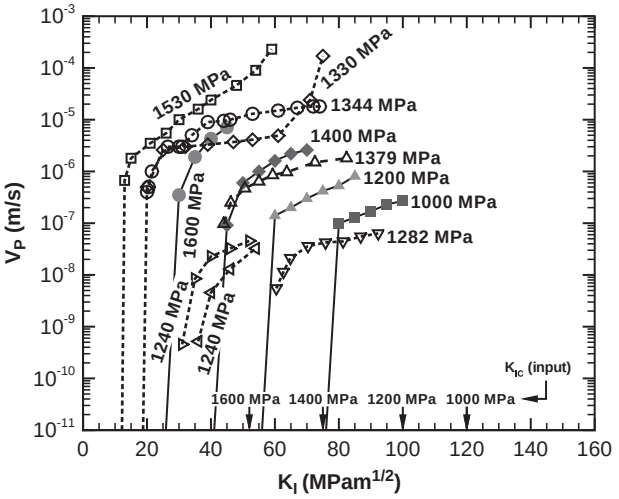

Fig. 11. Fracture mechanics curves for AISI 4340 in aqueous solutions. Filled symbols/solid lines: calculated, $C_{eq}(0) = 5.5 \times 10^{-6}$; open symbols/dashed lines: experimental; □, 1530 MPa, 0.1 N H_2SO_4 (Hirose and Mura, 1984b); ◇, 1330 MPa, 0.1 N H_2SO_4 (Hirose and Mura, 1984a); ◯, 1344 MPa, H_2O (Simmons et al., 1978); △, 1379 MPa, 3.5% NaCl (Colangelo and Ferguson, 1969); ▽, 1282 MPa, 3.5% NaCl (Colangelo and Ferguson 1969); ◁,▷, 1240 MPa, 3.5% NaCl (Lisagor, 1984).

Simmons et al., 1978; Colangelo and Ferguson, 1969; Lisagor, 1984). It is apparent that the scatter in the experimental data is quite considerable, and it may lead to particular experiments opposing the general trend (e.g., compare curves for 1344 and 1379 MPa). For purposes of comparison, a statistically meaningful data sample gleaned from many experiments needs to be employed, and an overall trend has to be extracted (cf., Sandoz, 1972; Gangloff, 1986). The simulations capture both qualitatively and quantitatively two basic features depicted in Fig. 3, namely: the existence of a threshold stress intensity and a plateau in the propagation rate. In addition, the model also reproduces the observed shift of the $V_P - K$ curves to lower K and to higher V_P with increasing yield strength.

Fig. 12 shows the variation of the threshold K_{SCC} on σ_{y0} that can be deduced from the onsets of cracking in Fig. 11. We see that the predicted threshold stress intensity factors lie within known experimental ranges (Sandoz, 1972; Brown, 1977), the agreement appearing better for the low end of the range. Experiments comparing high-strength steels of the series 41xx and 43xx with varying yield strengths (Beachem, 1972; Gerberich et al., 1988, González et al., 1996) in the presence of hydrogen sources reveal that varying the yield strength induces a change in cracking morphology, with transgranular quasicleavage dominating at low strength and intergranular fracture prevailing at high strength. Moreover, the transition occurs at about 1400 MPa, the strength above which the agreement between experiments and our calculations degrades. Since the cohesive law used in calculations is appropriate for the regime of transgranular fracture, we

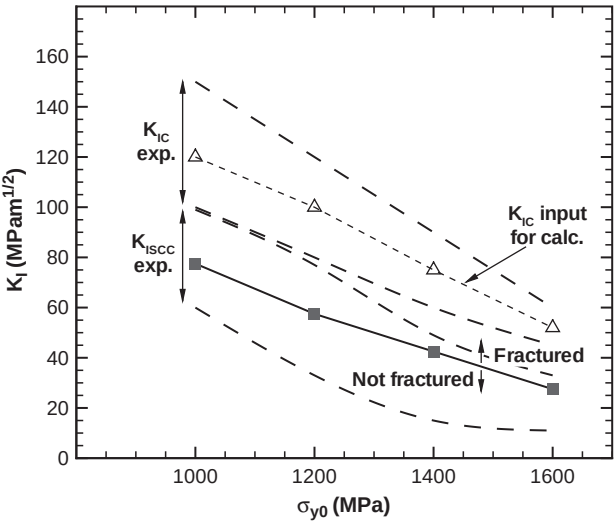

Fig. 12. Threshold stress intensity values for AISI 4340 steel in inert media and aqueous solutions. Closed symbols/solid lines: calculated, $C_{eq}(0)=5.5\times10^{-6}$; long-dashed lines: experimental ranges for K_C and K_{SCC} (Sandoz, 1972; Brown, 1977); open symbols/dotted lines: input K_C.

should expect deviations from experiment at high yield strength. Better agreement with experiment may conceivably be obtained by using different cohesive properties in the transgranular and intergranular regimes, but this enhancement of the model will not be pursued here.

Fig. 13 displays the effect of yield strength on stage II crack propagation rate. The experimentally observed increase in $V_{P,II}$ with σ_{y0} is captured by the simulations, though the predicted dependence of $V_{P,II}$ on σ_{y0} is weaker than measured values suggest. The trend is correct, namely, with increasing σ_{y0} interface cohesion becomes poorer either in the virgin or the embrittled state and stresses and stress gradients become higher, leading to a higher $V_{P,II}$. The discrepancy in slope between experiment and theory may again be due to the aforementioned transition in crack morphology with yield strength, which is not accounted for in the present implementation of the model. The lack of data for low σ_{y0} impedes a definitive comparison. The agreement jointly displayed in Figs. 11–13 is quite remarkable and lends credence to the model.

Fig. 14 illustrates the effect of hydrogen concentration in the environment, given by the bulk hydrogen concentration at a stress-free crack flank in equilibrium with the environment $C_{eq}(0)$ (Eq. (15)), on cracking thresholds. Turning to the experimental ranges shown, Fig. 14 contains the data compiled by Gangloff (1986) for several high-strength steels with $\sigma_{y0}=(1400\pm80)$ MPa, where we have removed the scaling factor $\exp(pV_H/RT)$ applied to the concentrations by Gangloff to account for stress effects, in order to directly compare with our calculations of the concentration at a stress-free surface. Gangloff separated the results between aqueous and gaseous environments, and we show the ranges of K_{SCC} for both cases. A lower slope is observed

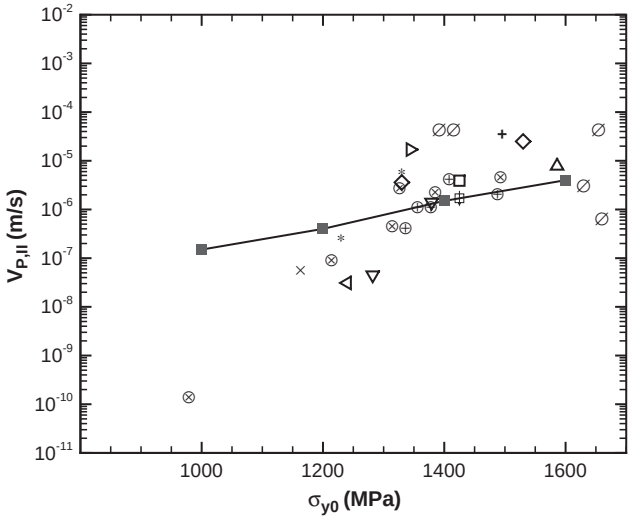

Fig. 13. Effect of yield strength σ_{y0} on plateau velocity $V_{P,II}$. Closed squares/solid line: calculated, $C_{eq}(0) = 5.5 \times 10^{-6}$; other symbols: experimental data; $\bigtriangledown$, V-4340, 3.5% NaCl (Colangelo and Ferguson, 1969); $*$, 4130, H_2O, 40 MPa $\sqrt{m}$, (Nelson and Williams, 1977); $\diamond$, 0.1 N H_2SO_4, 40 MPa $\sqrt{m}$ (Hirose and Mura, 1984a); $\triangleleft$, 4340, 3.5% NaCl (Lisagor, 1984); $\triangleright$, 4340, H_2O (Simmons et al., 1978); $\triangle$, H11, H_2O (Johnson and Willner, 1965); $+$, 4340, H_2O (van der Sluys, 1969); $\times$, 4340, H_2O (Vogt, 1997); $\otimes$, 4340 (Carter, 1971a); $\oplus$, 4340-Si, 3.5% NaCl (Carter, 1969); $\varnothing$, 4340-Si, 3.5% NaCl (Carter, 1969); $\square$, 4340, H_2O (Carter, 1971b); Φ, 4340, 3.0 N NaCl (Carter, 1971b).

for aqueous environments, i.e., for high concentration. Farrell (1970) observed a similar saturation of embrittlement at $C_{eq}(0) = 1.65 \times 10^{-4}$ for internal hydrogen embrittlement in unnotched samples. The simulations for $\sigma_{y0} = 1400$ MPa show a decrease in K_{SCC} when increasing $C_{eq}(0)$, and a plateau for the largest concentrations. The same qualitative behavior appears in experiments and simulations, namely a weaker dependence of K_{SCC} at high concentration. We note here that the experimental ranges quoted for $\sigma_{y0} = 1400$ MPa and $C_{eq}(0) = 5.5 \times 10^{-6}$ in Figs. 12 and 14 are not the same, as they include different sets of data.

Fig. 14 also shows the Langmuir–McLean isotherm used for the calculation of interface coverages. Above a concentration of 10^{-4}, the interface is close to saturated in hydrogen, with further increases in $C_{eq}(0)$ not having a significant effect. The calculated saturation of K_{SCC} with prescribed $C_{eq}(0)$ is a reflection of the interface saturation, and this can be readily confirmed by the Γ or $\theta = \Gamma/\Gamma_s$ profiles for K just below threshold. When $C_{eq}(0) = 5.5 \times 10^{-6}$, the limiting profile for $K = 40$ MPa $\sqrt{m}$ shows that $\theta \leqslant 0.73$ ML all along the interface, which is therefore not saturated, while for $C_{eq}(0) = 5.5 \times 10^{-5}$ and $K = 25$ MPa $\sqrt{m}$, $\theta \geqslant 0.92$ ML, almost saturated everywhere. We propose that the break in the experimental $\log K_{SCC} - \log C_{eq}(0)$ curve is related to saturation of the cracking interface, which is quantitatively found in our simulations, and not to the type of environment. It is conceivable that agreement for high concentrations might be improved by the consideration of different adsorption

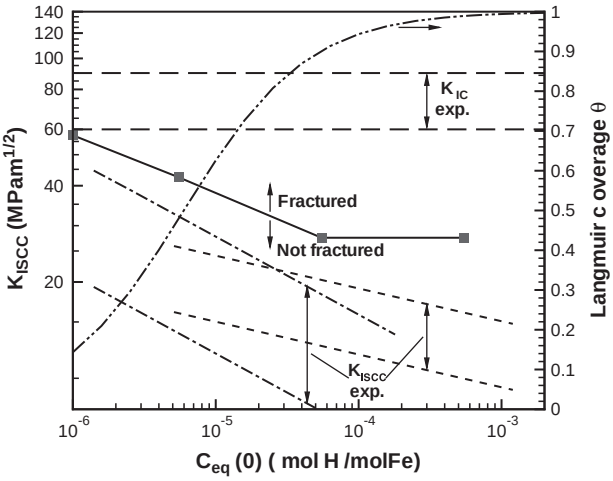

Fig. 14. Effect of subsurface equilibrium hydrogen concentration corresponding to a stress-free crack flank, $C_{eq}(0)$, on K_{SCC} (left vertical axis) and on Langmuir surface coverage, Eq. (18) (right vertical axis). All plots correspond to the left axis, except the plot of θ. Symbols/solid line: calculated, $\sigma_{y0} = 1400$ MPa; dash –dotted lines: experimental range, gaseous environment (Gangloff, 1986); short-dashed lines: experimental range, aqueous environment (Gangloff, 1986); long-dashed lines: experimental range of K_C.

sites at the cracking interface with a distribution of adsorption energies. Such multiple adsorption energies are specially likely to arise at high-angle grain boundaries (Myers et al., 1992). Our calculated threshold values are comparable to those measured in experiments in both gaseous and aqueous environments, since K_{SCC} is independent of the assumed rate-determining step, enabling the preceding analysis. On the other hand, $V_P - K$ curves and the derived $V_{P,II}$, which are related to kinetic phenomena, are not expected to agree with experimental results in gaseous media, where surface phenomena not accounted for in our model may be rate-determining (e.g., Nelson et al., 1970).

A remarkable result from the foregoing analysis is the necessity of a saturating embrittlement law, as the Langmuir–McLean isotherm provides. Embrittlement laws are often given in terms of a critical fracture stress $\bar{\sigma}_c$ dependent on the local bulk hydrogen concentration C (Oriani and Josephic, 1974). This dependence is sometimes assumed to be linear (Oriani and Josephic, 1974; Akhurst and Baker, 1981; Gerberich et al., 1988), i.e., of the form $\bar{\sigma}_c(C) = \bar{\sigma}_{c0} - \lambda C$, where $\bar{\sigma}_{c0} = \bar{\sigma}_c(0)$ is the intrinsic value. This form predicts the complete decohesion of interfaces upon the attainment of a certain critical value of C, leading to $K_{SCC} = 0$ for sufficiently aggressive environments. Based on our findings, this type of embrittlement law should be replaced by one exhibiting saturation, as is obtained from the composition of Eqs. (8) and (18).

3.2. Effect of temperature

For many systems, the dependence of $V_{P,II}$ on temperature T is bell-shaped, and displays a typical Arrhenius profile at low temperature along with a sharp downturn at

high temperature. At present, there is no general agreement on the precise nature of the rate determining steps (RDS) underlying the observed behavior. For instance, for internal hydrogen, where surface phenomena plays no role, and H_2 gaseous environment, some authors (Gerberich et al., 1988; Chen and Gerberich, 1991) simply treat the transition temperature T_0 as an empirical parameter to be determined from experiment. Furthermore, they introduce explicitly the effect of temperature on an effective diffusion coefficient, implying diffusion rate control at low temperature and an unknown process at high temperature. By way of contrast, Simmons et al. (1978) posit surface reaction as the low-temperature RDS in aqueous environment, and an unspecified step for H_2 environment. Nelson et al. (1970) propose that the high-temperature RDS in H_2 is surface reaction, while at low temperature they suggest that diffusion transport is not a limiting factor.

In the present model, the temperature dependence of environment-assisted cracking and, in particular, stage II crack-propagation rates, is due to a number of factors, including: (i) the equilibrium bulk hydrogen concentration; (ii) the hydrogen coverage at the cracking interface; (iii) the effective diffusion constant; and (iv) the mechanical properties of the host. Assuming a constant equivalent hydrogen gas pressure in the environment, the equilibrium concentration of bulk hydrogen at zero stress and temperature T is

$$C_{\mathrm{eq}}(0,T) = C_{\mathrm{eq}}(0,T^*)\exp\left(-\frac{\Delta H_{\mathrm{s}}}{R}\left(\frac{1}{T}-\frac{1}{T^*}\right)\right), \tag{22}$$

where the heat of solution $\Delta H_{\mathrm{s}} = 28.6$ kJ/mol is considered temperature-independent (Hirth, 1980), and T^* is any reference temperature for which $C_{\mathrm{eq}}(0)$ is known. C_{eq} is also affected by temperature through the exponential factor of Eq. (15). The equilibrium between the hydrogen surface concentration at the cracking interface and the adjoining bulk material depends on temperature through Eq. (18).

The temperature dependence of the diffusion coefficient is similar to that expressed by Eq. (22), namely,

$$D_{\mathrm{eff}}(T) = D_{\mathrm{eff},0}\exp\left(-\frac{\Delta H_{\mathrm{d}}}{RT}\right) = D_{\mathrm{eff}}(T^*)\ \exp\left(-\frac{\Delta H_{\mathrm{d}}}{R}\left(\frac{1}{T}-\frac{1}{T^*}\right)\right), \tag{23}$$

with ΔH_{d}=40 kJ/mol (Turnbull et al., 1995). A combination of $D_{\mathrm{eff},0}=1.2\times10^{-7}$ m^2/s, corresponding to pure iron, and $\Delta H_{\mathrm{d}}=40$ kJ/mol, was used by Gerberich et al. (1988) to fit $V_{\mathrm{P,II}}$ values, but this choice gives $D_{\mathrm{eff}} = 10^{-14}$ m^2/s at room temperature, orders of magnitude lower than measured values. This discrepancy exemplifies the risk of using $D_{\mathrm{eff},0}$, as in the second member of Eq. (23), instead of $D_{\mathrm{eff}}(T^*)$.

We additionally assume the power softening law

$$\sigma_{\mathrm{y0}}(T) = \sigma_{\mathrm{y0}}(T^*)\left(\frac{T-T_{\mathrm{m}}}{T^*-T_{\mathrm{m}}}\right)^q, \tag{24}$$

for the yield stress, with the exponents given in Table 1, which fits well the experimentally determined temperature dependence of 4340 steel in the range -25°C to 200°C (Larson and Nunes, 1961). As before, T^* is a reference temperature for which

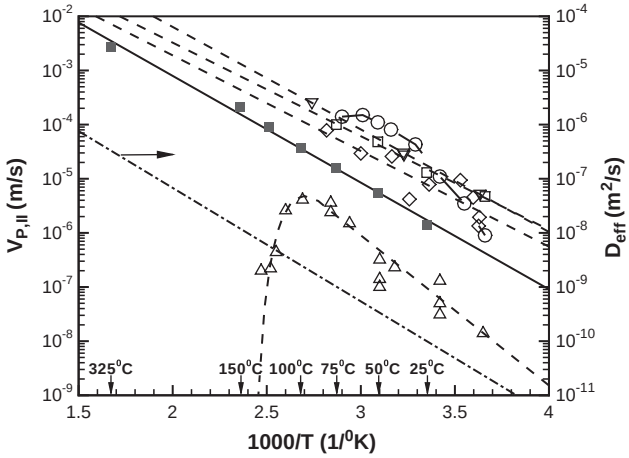

Fig. 15. Effect of temperature on stage II crack velocity (left vertical axis) and effective diffusion coefficient (right vertical axis). Solid symbols: calculated, $\sigma_{y0} = 1400$ MPa, $K = 60$ MPa $\sqrt{\text{m}}$, $C_{eq}(0) = 5.5 \times 10^{-6}$; open symbols/dashed lines: experimental; □, 4340, 1344 MPa, H_2O (Simmons et al., 1978); ◇, H11, 1586 MPa, H_2O (Johnson and Willner, 1965); ▽, 4340, 1496 MPa, H_2O (van der Sluys, 1969); ◯, 4130, 1330 MPa, H_2O (Nelson and Williams, 1977); △, 4340, 1163 MPa, H_2O (Vogt, 1997).

the value of $\sigma_{y0}(T^*)$ is known (e.g., for room temperature the yield strength is given in Table 1), and $T_m = 1808$ K, the melting point of iron (Shackleford and Alexander, 1992).

Fig. 15 displays the temperature dependence of stage II crack-propagation rates, for $\sigma_{y0} = 1400$ MPa and $K = 60$ MPa $\sqrt{\text{m}}$, as well as the temperature dependence of D_{eff}. The slope of the $V_{P,II}$ line yields an activation energy for the crack velocity $E_{a,V_{P,II}} = 41.0$ kJ/mol for 25–150°C, only 1.0 kJ/mol higher than that for D_{eff}. The contribution of yield stress softening is small over this temperature range, and the same applies to the effect of local tensile stress (Eq. (15)). This is due to the fact that the embrittlement process acts over a region where the exponential factor of Eq. (15) varies at most by a factor of two, within the range of temperatures considered. Thus, it appears that the temperature dependence of the bulk equilibrium concentration of hydrogen at zero stress and the surface coverage at the cracking interface compensate each other. This is expected in view of the similar values of ΔH_s and Δg_b^0, leading to the net observed $E_{a,V_{P,II}} \approx \Delta H_d$. Diffusion affected by trapping, included here via an effective diffusion coefficient, is thus a likely rate determining step for HE.

The experimentally observed downturn in $V_{P,II}$ with increasing temperature above 100°C is not reproduced by our model, suggesting that a mechanism not accounted for is involved and ruling out thermal softening as the main cause. It appears that no mechanism has been proposed to explain the high temperature behavior to date, and only phenomenological models (Gao and Wei, 1985) are available.

4. Summary and concluding remarks

We have constructed a continuum model informed by quantum mechanical calculations for the simulation of hydrogen embrittlement in metals. The key features include: (i) cohesive surfaces described by concentration-dependent constitutive relations derived from first principles quantum mechanics; (ii) stress-assisted impurity diffusion; (iii) impurity coverage at the incipient crack surfaces determined from the Langmuir relation; and (iv) continuum finite element modeling including plasticity.

The model provides qualitative and quantitative predictions of a number of experimental observations. Thus, the calculated crack initiation times, and their dependence on applied stress intensity and yield strength, are consistent with measured values and trends. In addition, the model predicts a crack jump at initiation the size of which is in good agreement with measured initial jump lengths. During crack propagation, the model predicts intermittent crack growth, consisting of discrete jumps separated by quiescent periods during which the crack is stationary. The calculated sizes of the discrete jumps executed by the crack are in good agreement with measurements. At the microscale, the model suggests that the intermittency of cracking is controlled by the rate at which bulk hydrogen is able to diffuse to the embrittlement region.

The model enables the calculation of fracture curves characteristic of environment-assisted cracking, e.g., the crack propagation rate V_P as a function of the applied stress intensity factor K. The calculated curves exhibit a number of features, such as thresholds and plateaus, which are in good qualitative agreement with experimental trends. A strong effect of yield strength is predicted, in keeping with observation. The fidelity of the model deteriorates for regimes where grain boundary decohesion is important, as this effect is not accounted for explicitly at present. Examination of the computed effect of concentration on cracking thresholds suggests the need for a saturation regime in the embrittlement law. Lastly, the model reproduces the effect of temperature on stage II crack propagation, namely, an increase in crack velocity with increasing temperature, although the experimentally observed downturn in $V_{P,II}$ at higher temperatures is not reproduced. The calculated activation energy for stage II crack-propagation rate coincides with the activation energy for diffusion of hydrogen.

Overall, the agreement between the model and experimental data is compelling enough to suggest that hydrogen-induced decohesion may be the dominant mechanism of hydrogen-assisted fracture for high-strength steels in aqueous environments.

Some further developments of the model may be of interest. Full three-dimensional simulation may account for nonuniform crack advancement and possibly ligament tearing. The model may also be modified to test other embrittlement mechanisms, such as HELP, thereby allowing a more definitive assessment of the relative importance of the various mechanisms.

Acknowledgements

E.A.C. and M.O. are grateful to the US Department of Defense for support provided through Brown University's MURI Center for the "Design and Testing of Materials by

Computation: A Multi-Scale Approach." E.A.C. also acknowledges the Army Research Office for partial support. M.O. acknowledges the Office of Naval Research for partial support provided under grant N00014-96-1-0068.

References

Akhurst, K.N., Baker, T.J., 1981. The threshold stress intensity for hydrogen-induced crack growth. Metall. Trans. A—Phys. Metall. Mater. Sci. 12A (6), 1059–1070.

Barenblatt, G.I., 1962. The mathematical theory of equilibrium of crack in brittle fracture. Adv. Appl. Mech. 7, 55–129.

Beachem, C.D., 1972. A new model for hydrogen-assisted cracking (hydrogen "embrittlement"). Metall. Trans. 3 (2), 437–451.

Beltz, G.E., Rice, J.R., Shih, C., Xia, L., 1996. A self-consistent model for cleavage in the presence of plastic flow. Acta Mater. 44 (10), 3943–3954.

Birnbaum, H.K., 1990. Mechanisms of Hydrogen-Related Fracture of Metals. In: Gangloff, R.P., Ives, M.B. (Eds.), First International Conference on Environment-induced Cracking of Metals, NACE-10. NACE, Houston, TX, pp. 21–27.

Birnbaum, H.K., Sofronis, P., 1994. Hydrogen-enhanced localized plasticity—A mechanism for hydrogen-related fracture. Mater. Sci. Eng. A—Struct. Mater. Prop. 176A (1–2), 191–202.

Brown, B.F., 1977. High strength steels. In: Brown, B.F. (Ed.), Stress Corrosion Cracking Control Measures, NBS Monograph 156. National Bureau of Standards, Washington, DC, pp. 43–54 (Chapter 6).

Camacho, G.T., Ortiz, M., 1996. Computational modelling of impact damage in brittle materials. Int. J. Solid Struct. 33 (20–22), 2899–2938.

Carter, C.S., 1969. The effect of silicon on the stress corrosion resistance of low alloy high strength steels. Corrosion 25 (10), 423–431.

Carter, C.S., 1971a. Fracture toughness and stress corrosion characteristics of a high strength maraging steel. Metall. Trans. 2 (6), 1621–1626.

Carter, C.S., 1971b. Observations on the stress corrosion crack propagation characteristics of high strength steels. Corrosion 27 (11), 471–477.

Chen, X., Gerberich, W.W., 1991. The kinetics and micromechanics of hydrogen-assisted cracking in Fe-3 pct Si single crystals. Metall. Trans. A—Phys. Metall. Mater. Sci. 22A (1), 59–70.

Colangelo, V.J., Ferguson, M.S., 1969. The role of strain hardening exponent in stress corrosion cracking of a high strength steel. Corrosion 25 (12), 509–514.

Doig, P., Jones, G.T., 1977. Model for initiation of hydrogen embrittlement cracking at notches in gaseous hydrogen environments. Metall. Trans. A—Phys. Metall. Mater. Sci. 8 (12), 1993–1998.

Dugdale, D.S., 1960. Yielding of steel sheets containing slits. J. Mech. Phys. Solids 8 (2), 100–104.

Edeleanu, C., Forty, A.J., 1960. Some observations on the stress-corrosion cracking of α-brass and similar alloys. Philos. Mag. 5 (58), 1029–1040.

Farrell, K., 1970. Cathodic hydrogen absorption and severe embrittlement in a high strength steel. Corrosion 26 (3), 105–110.

Ford, P.E., 1990. The Crack Tip System and its Relevance to the Prediction of Cracking in Aqueous Environments. In: Gangloff, R.P., Ives, M.B. (Eds.), First International Conference on Environment-induced Cracking of Metals, NACE-10. NACE, Houston, TX, pp. 139–166.

Fukai, Y., 1993. The Metal-Hydrogen System: Basic Bulk Properties. Springer, Berlin.

Galvele, J.R., 1981. Transport processes in passivity breakdown—II. Full hydrolysis of the metal ions. Corrosion Sci. 21 (8), 551–579.

Galvele, J.R., 1987. A stress corrosion cracking mechanism based on surface mobility. Corrosion Sci. 27 (1), 1–33.

Galvele, J.R., 2000. Recent developments in the surface-mobility stress–corrosion–cracking mechanism. Electrochim. Acta 45 (21), 3537–3541.

Gangloff, R.P., 1986. A review and analysis of the threshold for hydrogen environment embrittlement of steel. In: Levy, M., Isserow, S. (Eds.), Corrosion Prevention and Control: Proceedings of the 33rd Sagamore Army Materials Research Conference. US Army Laboratory Command, Watertown, MA, pp. 64–111.

Gangloff, R.P., Ives, M.B. (Eds.), 1990. First International Conference on Environment-induced Cracking of Metals, NACE-10. NACE, Houston, TX.

Gao, M., Wei, R.P., 1985. A "hydrogen partitioning" model for hydrogen assisted crack growth. Metall. Trans. A—Phys. Metall. Mater. Sci. 16A (11), 2039–2050.

Gao, M., Lu, M., Wei, R.P., 1984. Crack paths and hydrogen-assisted crack-growth response in AISI-4340 steel. Metall. Trans. A—Phys. Metall. Mater. Sci. 15 (4), 735–746.

Gerberich, W.W., Livne, T., Chen, X.-F., Kaczorowski, M., 1988. Crack growth from internal hydrogen—Temperature and microstructural effects in 4340 steel. Metall. Trans. A—Phys. Metall. Mater. Sci. 19A (5), 1319–1334.

González, J., Gutiérrez-Solana, F., Varona, J.M., 1996. The effect of microstructure, strength level, and crack propagation mode on stress corrosion cracking behavior of 4135 steel. Metall. Mater. Trans. A—Phys. Metall. Mater. Sci. 27A (2), 281–290.

Hayes, R.L., Ortiz, M., Carter, E.A., 2004. Universal binding-energy relation for crystals that account for surface relaxation. Phys. Rev. B 69, 172104.

Hirose, Y., Mura, T., 1984a. Growth mechanism of stress corrosion cracking in high strength steel. Eng. Fract. Mech. 19 (6), 1057–1067.

Hirose, Y., Mura, T., 1984b. Nucleation mechanism of stress-corrosion cracking from notches. Eng. Fract. Mech. 19 (2), 317–329.

Hirth, J.P., 1980. Effect of hydrogen on the properties of iron and steel. Metall. Trans. A—Phys. Metall. Mater. Sci. 11A (6), 861–890.

Hondros, E.D., Seah, M.P., 1977. Theory of grain-boundary segregation in terms of surface adsorption analogs. Metall. Trans. A—Phys. Metall. Mater. Sci. 8 (9), 1363–1371.

Jiang, D.E., Carter, E.A., 2004a. Diffusion of interstitial hydrogen into and through bcc Fe from first principles. Phys. Rev. B 70, 064102.

Jiang, D.E., Carter, E.A., 2004b. First principles assessment of hydrogen embrittlement in Fe and Al crystals. Phys. Rev. B, to be submitted.

Johnson, H.H., Willner, A.M., 1965. Moisture and stable crack growth in a high strength steel. Appl. Mater. Res. 4, 34–40.

Jokl, M.L., Vitek, V., McMahon, C.J., 1980. A microscopic theory of brittle-fracture in deformable solids—A relation between ideal work to fracture and plastic work. Acta Metall. 28 (11), 1479–1488.

Jones, R.H. (Ed.), 2001. Chemistry and Electrochemistry of Corrosion and Stress Corrosion Cracking: A Symposium Honoring the Contributions of R.W. Staehle. TMS, Warrendale, PA.

Kerns, G.E., Wang, M.T., Staehle, R.W., 1977. Stress Corrosion Cracking and Hydrogen Embrittlement in High Strength Steels. In: Staehle, R.W., Hochmann, J., McCright, R.D., Slater, J.E. (Eds.), Stress Corrosion Cracking and Hydrogen Embrittlement of Iron Based Alloys, NACE-5. NACE, Houston, TX, pp. 700–735.

Larson, F.R., Nunes, J., 1961. Low temperature flow and fracture tension properties of heat-treated SAE 4340 steel. Trans. ASM 53, 663–682.

Larson, F.R., Nunes, J., 1962. Relationships between energy, fibrosity, and temperature in charpy impact tests on AISI 4340 steel. Proc. ASTM 62, 1192–1209.

Lee, S.L., Unger, D.J., 1988. A decohesion model of hydrogen assisted cracking. Eng. Fract. Mech. 31 (4), 647–660.

Lisagor, W.B., 1984. Influence of precracked specimen configuration and starting stress intensity on the stress corrosion cracking of 4340 steel. In: Dean, S.W., Pugh, E.N., Ugiansky, G.M. (Eds.), Environment-sensitive Fracture—Evaluation and Comparison of Test Methods. ASTM, Philadelphia, PA, pp. 80–97.

Lu, M., Pao, P.S., Weir, T.W., Simmons, G.W., Wei, R.P., 1981. Rate controlling processes for crack growth in hydrogen sulfide for an AISI 4340 steel. Metall. Trans. A—Phys. Metall. Mater. Sci. 12A (5), 805–811.

Marsh, P., Gerberich, W.W., 1992. Stress corrosion cracking of high-strength steels. In: Jones, R.H. (Ed.), Stress-corrosion Cracking. ASM International, Materials Park, OH, pp. 63–90.

Myers, S.M., Baskes, M.I., Birnbaum, H.K., Corbett, J.W., DeLeo, G.G., Estreicher, S.K., Haller, E.E., Jena, P., Johnson, N.M., Kirchheim, R., Pearton, S.J., Stavola, M.J., 1992. Hydrogen interactions with defects in crystalline solids. Rev. Mod. Phys. 64 (2), 559–617.

Nelson, H.G., 1976. Film-rupture model of hydrogen-induced, slow crack growth in acicular alpha-beta titanium. Metall. Trans. A—Phys. Metall. Mater. Sci. 7A (5), 621–627.

Nelson, H.G., Williams, D.P., 1977. Quantitative Observations of Hydrogen-induced Slow Crack Propagation in a Low Alloy Steel. In: Staehle, R.W., Hochmann, J., McCright, R.D., Slater, J.E. (Eds.), Stress Corrosion Cracking and Hydrogen Embrittlement of Iron Based Alloys, NACE-5. NACE, Houston, TX, pp. 390–404.

Nelson, H.G., Williams, D.P., Tetelman, A.S., 1970. Embrittlement of a ferrous alloy in a partially dissociated hydrogen environment. Metall. Trans. 2 (4), 953–959.

Nguyen, O.T., 2000. Cohesive models of fatigue crack growth and stress-corrosion cracking. Ph.D. Thesis, California Institute of Technology, Pasadena, CA.

Nguyen, O., Ortiz, M., 2002. Coarse-graining and renormalization of atomistic binding relations and universal macroscopic cohesive behavior. J. Mech. Phys. Solids 50 (8), 1727–1741.

Nguyen, O., Repetto, E.A., Ortiz, M., Radovitzky, R., 2001. A cohesive model of fatigue crack growth. Int. J. Fract. 110 (4), 351–369.

Oriani, R.A., 1970. The diffusion and trapping of hydrogen in steel. Acta Metall. 18 (1), 147–157.

Oriani, R.A., 1972. Mechanistic theory of hydrogen embrittlement of steels. Ber. Bunsenges. Phys. Chem. 76 (8), 848–857.

Oriani, R.A., 1990. Hydrogen Effects in High-strength Steels. In: Gangloff, R.P., Ives, M.B. (Eds.), First International Conference on Environment-induced Cracking of Metals, NACE-10. NACE, Houston, TX, pp. 439–447.

Oriani, R.A., Josephic, P.H., 1974. Equilibrium aspects of hydrogen-induced cracking of steels. Acta Metall. 22 (9), 1065–1074.

Oriani, R.A., Josephic, P.H., 1977. Equilibrium and kinetic studies of the hydrogen-assisted cracking of steels. Acta Metall. 25 (9), 979–988.

Ortiz, M., Pandolfi, A., 1999. Finite deformation irreversible cohesive elements for three-dimensional crack-propagation analysis. Int. J. Numer. Methods Eng. 44 (9), 1267–1282.

Page, R.A., Gerberich, W.W., 1982. The effect of hydrogen source on crack initiation in 4340-steel. Metall. Trans. A—Phys. Metall. Mater. Sci. 13 (2), 305–311.

Park, K.C., Felippa, C.A., 1983. Partitioned analysis of coupled systems. In: Belytschko, T., Hughes, T.J.R. (Eds.), Computational Methods for Transient Analysis. Vol. A1: Mechanics and Mathematical Methods —Series of Handbooks. Elsevier Science, Englewood Cliffs, NJ, pp. 157–219 (Achenbach, J.D. general editor).

Parkins, R.N., 1990. Stress Corrosion Cracking. In: Gangloff, R.P., Ives, M.B. (Eds.), First International Conference on Environment-induced Cracking of Metals, NACE-10. NACE, Houston, TX, pp. 1–20.

Porter, D.A., Easterling, K.E., 1981. Phase Transformations in Metals and Alloys. Chapman & Hall, London, pp. 92–93 (Chapter 2).

Pound, B.G., 1998. Hydrogen trapping in high-strength steels. Acta Mater. 46 (16), 5733–5743.

Rice, J.R., 1968. Mathematical analysis in the mechanics of fracture. In: Leibowitz, H. (Ed.), Fracture—An Advanced Treatise. Vol. 2: Mathematical Fundamentals. Academic Press, New York, NY, pp. 192–308. (Chapter 3).

Rice, J.R., Wang, J.-S., 1989. Embrittlement of interfaces by solute segregation. Mater. Sci. Eng. A—Struct. Mater. Prop. 107, 23–40.

Rose, J.H., Smith, J.R., Guinea, F., Ferrante, J., 1984. Universal features of the equation of state of metals. Phys. Rev. B 29 (6), 2963–2969.

Sandoz, G., 1972. High strength steels. In: Brown, B.F. (Ed.), Stress-Corrosion Cracking in High Strength Steels and in Titanium and Aluminum Alloys. Naval Research Laboratory, Washington, DC, pp. 79–145 (Chapter 3).

Scully, J.C., 1975. Stress corrosion crack propagation: a constant charge criterion. Corrosion Sci. 15 (4), 207–224.

Scully, J.R., Moran, P.J., 1988. The influence of strain on hydrogen entry and transport in a high strength steel in sodium chloride solution. J. Electrochem. Soc. 135 (6), 1337–1348.

Shackleford, J.F., Alexander, W. (Eds.), 1992. The CRC Materials Science and Engineering Handbook. CRC Press, Boca Raton, FL, p. 21.

Sharland, S.M., Tasker, P.W., 1988. A mathematical model of crevice and pitting corrosion—I. The physical model. Corrosion Sci. 28 (6), 603–620.

Sieradzki, K., Newman, R.C., 1985. Brittle behaviour of ductile metals during stress-corrosion cracking. Philos. Mag. A 51 (1), 95–132.

Sieradzki, K., Newman, R.C., 1987. Stress-corrosion cracking. J. Phys. Chem. Solids 48 (11), 1101–1113.

Simmons, G.W., Pao, P.S., Wei, R.P., 1978. Fracture mechanics and surfacechemistry studies of subcritical crack growth in AISI 4340 steel. Metall. Trans. A—Phys. Metall. Mater. Sci. 9A (8), 1147–1158.

Sofronis, P., 2001. Recent advances in the engineering aspects of hydrogen embrittlement—Special number. Eng. Fract. Mech. 68 (6), 617–837.

Sofronis, P., McMeeking, R.M., 1989. Numerical analysis of hydrogen transport near a blunting crack tip. J. Mech. Phys. Solids 37 (3), 317–350.

Suo, Z., Shih, C.F., Varias, A.G., 1993. A theory for cleavage cracking in the presence of plastic-flow. Acta Metall. Mater. 41 (5), 1551–1557.

Taha, A., Sofronis, P., 2001. A micromechanics approach to the study of hydrogen transport and embrittlement. Eng. Fract. Mech. 68 (6), 803–837.

Troiano, A.R., 1960. The role of hydrogen and other interstitials in the mechanical behavior of metals. Trans. ASM 52, 54–80.

Turnbull, A., 1993. Modeling of environment assisted cracking. Corrosion Sci. 34 (6), 921–960.

Turnbull, A., 2001. Modeling of the chemistry and electrochemistry in cracks—a review. Corrosion 57 (2), 175–189.

Turnbull, A., Saenz de Santa Maria, M., 1988. Predicting the kinetics of hydrogen generation at the tips of corrosion fatigue cracks. Metall. Trans. A—Physical Metall. Mater. Sci. 19 (7), 1795–1806.

Turnbull, A., Lembach-Beylegaard, E., Hutchings, R.B., 1995. Hydrogen transport in SAF 2205 and SAF 2507 duplex stainless steel. In: Turnbull, A. (Ed.), Hydrogen Transport and Cracking in Metals. The Institute of Materials, Cambridge, UK, pp. 268–279.

Turnbull, A., Ferriss, D.H., Anzai, H., 1996. Modelling of the hydrogen distribution at a crack tip. Mater. Sci. Eng. A—Struct. Mater. Prop. 206 (1), 1–13.

Tvergaard, V., 1997. Cleavage crack growth resistance due to plastic flow around a near-tip dislocation-free region. J. Mech. Phys. Solids 45 (6), 1007–1023.

Tvergaard, V., 1998. Effect of T-stress on the cleavage crack growth resistance resulting from plastic flow. J. Phys. IV 8 (P8), 391–398.

Tvergaard, V., Hutchinson, J.W., 1992. The relation between crack growth resistance and fracture process parameters in elastic–plastic solids. J. Mech. Phys. Solids 40 (6), 1377–1397.

Unger, D.J., 1989. A mathematical analysis for impending hydrogen assisted crack propagation. Eng. Fract. Mech. 34 (3), 657–667.

van der Sluys, W.A., 1969. Mechanisms of environment induced subcritical flaw growth in AISI 4340 steel. Eng. Fract. Mech. 1, 447–462.

van der Ven, A., Ceder, G., 2003. Impurity induced van der Waals transition during decohesion. Phys. Rev. B 67 (6), 060101.

van Leeuwen, H.P., 1975. Plateau velocity of SCC in high strength steel—A quantitative treatment. Eng. Fract. Mech. 31 (2), 42–50.

Vermilyea, D.A., 1977. A Film Rupture Model for Stress Corrosion Cracking. In: Staehle, R.W., Hochmann, J., McCright, R.D., Slater, J.E. (Eds.), Stress Corrosion Cracking and Hydrogen Embrittlement of Iron Based Alloys, NACE-5. NACE, Houston, TX, pp. 208–217.

Vogt, H., 1997. Temperature dependency of stress corrosion cracking. Ph.D. Thesis, ETH, Swiss Federal Institute of Technology, Zurich, Switzerland, Dissertation ETH No. 12238.

Völkl, J., Alefeld, G. (Eds.), 1978. Hydrogen in Metals—Basic Properties. Topics in Applied Physics, Vol. 28. Springer, Berlin.

Wang, J.-S., Vehoff, H., 1991. The effect of the mobility of segregated atoms on interfacial embrittlement. Scr. Metall. Mater. 25 (6), 1339–1344.

Westlake, D.G., 1969. A generalized model for hydrogen embrittlement. Trans. ASM 62 (4), 1000–1006.

Zhong, L.P., Wu, R.Q., Freeman, A.J., Olson, G.B., 2000. Charge transfer mechanism of hydrogen-induced intergranular embrittlement of iron. Phys. Rev. B 62 (21), 13938–13941.